Mn/N co-doped biochar-activated persulfate degradation of tetracycline in water

Haichen Cui
Nanjing Forestry University
Lu Li
Nanjing Water Group Co., Ltd.
Yannan Jia
China Institute of Water Resources and Hydropower Research
Nannan Xu
China Institute of Water Resources and Hydropower Research
Zheng Wang
wangzheng@njfu.edu.cn

Nanjing Forestry University
Zhendong Liu
Nanjing Water Group Co., Ltd.
Junchi Zhang
Nanjing Forestry University
Chenyue Zhang
Nanjing Forestry University
Weixiao Gong
Nanjing Forestry University
Wanting Feng
Nanjing Forestry University
Yuanxiang Shan
Nanjing Forestry University
Hongqin Xue
Nanjing Forestry University

Research Article

Keywords: Modified biochar, Mn/N co-doping, Persulfate degradation, Activation mechanism, Degradation efficiency, Organic pollutant, Mn/N-BC catalyst

Posted Date: May 13th, 2026

DOI: https://doi.org/10.21203/rs.3.rs-9365760/v1

Additional Declarations: No competing interests reported.

Mn/N co-doped biochar-activated persulfate degradation of tetracycline in water

Haichen Cui[1,2,3], Lu Li[4], Yannan Jia[2,3,*], Nannan Xu[2,3] , Zheng Wang[1,**] ,Zhendong Liu[4], Junchi Zhang[1],Chenyue Zhang[1],Weixiao Gong[1],Wanting Feng[1], Yuanxiang Shan[1],Hongqin Xue[1]

1. College of Civil Engineering, Nanjing Forestry University, Longpan Road 159#, Nanjing 210037, China;

2. State Key Laboratory of Water Cycle and Water Security in River Basin, China Institute of Water Resources and Hydropower Research, Beijing 100038,China;

3. China Institute of Water Resources and Hydropower Research, Beijing 100038, China;

4. Nanjing Water Group Co., Ltd., Zhongshan East Road 460#, Nanjing 210002, China

Corresponding authors at: College of Civil Engineering, Nanjing Forestry University, Longpan Road 159#, Nanjing 210037, China (Z.Wang) ; State Key Laboratory of Water Cycle and Water Security in River Basin, China Institute of Water Resources and Hydropower Research, Beijing 100038, China (Y. Jia).

E-mail addresses: wangzheng@njfu.edu.cn (Z. Wang), jiayn@iwhr.com (Y. Jia).

Abstract

Fresh sweet flag (*Acorus calamus*) biochar (BC) was modified by impregnation pyrolysis, and the ability of the resulting Mn/N-BC material to activate peroxydisulfate (PDS) adsorption and degrade tetracycline (TC) was investigated alongside its reaction mechanism. Under the optimal 1:1:1 BC:N:Mn doping ratio and optimal experimental conditions (2 mM PDS, 1.0 g/L catalyst dosage, pH 7), Mn/N-BC+PDS degraded 93.67% of 20 mg/mL TC within 120 min and maintained a removal rate of >80% after three cycles. Co-doping of two elements provided a large number of active sites for PDS

activation. Nitrogen was detected in the form of pyridine N, pyrrole N, and graphite N. Structural defects caused by doping in carbon materials generates $^1O_2$ non-free radicals, and loading of Mn breaks the O-O bond in PDS and produces $SO_4^{\bullet -}$ and •OH free radicals. These reactive substances play a role in degrading TC and other organic pollutants. Following treatment with the developed system, TC solutions exhibited reduced toxicity and potential feasibility for further exploration in water treatment.

Keywords: Modified biochar; Mn/N co-doping; Persulfate degradation; Activation mechanism; Degradation efficiency; Organic pollutant; Mn/N-BC catalyst

1. Introduction

Since the discovery of penicillin in 1928, antibiotics have emerged as a crucial class of antibacterial agents [1]. High levels of residual antibiotics in human and livestock feces pose significant environmental risks to agricultural soil and groundwater, and can stimulate antibiotic resistance genes (ARGs) and antibiotic resistant bacteria (ARB), threatening human and animal health [2-4]. Tetracycline (TC), a widely used antibiotic with an annual global production of thousands of tons, is considered a prominent emerging pollutant [5]. Its excellent chemical stability makes TC resistant to degradation by traditional biochemical or physicochemical treatments [6], and more efficient methods are being sought.

Among existing treatment methods, advanced oxidation processes (AOPs) can generate highly reactive free radicals such as •OH, $SO_4^{\bullet -}$, and $O_2^{\bullet -}$. AOPs can usually be divided into five types according to how free radicals are generated: ozone-based, ultraviolet-based, electrochemical, catalytic, and physical [7]. Among them, AOPs utilizing $SO_4^{\bullet -}$ with high redox potential (E_0 ranging from 2.5 to 3.1 V) and strong oxidation ability have broad application prospects [8, 9]. Peroxydisulfate (PDS) and peroxymonosulfate (PMS), collectively referred to as persulfate (PS) [10], can generate reactive free radicals through heating, ultraviolet radiation, ultrasound, carbon materials, transition metal oxides, ozone, and electrical activation [11, 12]. Carbon materials, notable for being inexpensive, not requiring additional energy, and recyclable, have received much attention [13].

Derived from biomass pyrolysis, biochar (BC) is an eco-friendly carbonaceous

material prized for its tunable specific surface area, high porosity, and abundant surface functional groups. Its application contributes to lowering greenhouse gas emissions, promoting carbon sequestration, recycling of waste resources, and innovative green development concepts [14]. Owing to its exceptional performance, BC is extensively utilized in agriculture, gas storage, and environmental remediation [15].

Raw BC has been modified by acid-base treatment [16], heteroatom doping [17, 18], metal ion loading [19, 20], and metal non-metal co-doping [21] to improve its catalytic efficacy. The present work employed fresh sweet flag (*Acorus calamus*) powder as a biomass precursor to prepare Mn/N-BC catalyst via impregnation pyrolysis. The effects of different doping levels of BC, Mn, and N on the efficiency of PDS-activated TC degradation were explored, and optimal catalyst preparation conditions were determined. Catalytic materials were prepared according to the optimal doping ratio, and factors influencing efficiency were analyzed experimentally to identify optimal experimental conditions for adsorption degradation.

2. Materials and methods

2.1. Experimental reagents

Raw *A. calamus* BC prepared in this experiment was purchased from Lishui, Foshan, Guangdong, China. Chemical reagents used in this study are listed in Table 1.

Table 1 Reagents used in this study

Reagent	Molecular formula	Specifications	Manufacturer

Tetracycline	$C_{22}H_{24}N_2O_8$	Analytical grade	Shanghai Macklin Biochemical Co., Ltd.
Sodium persulfate	$Na_2S_2O_8$		
Manganese chloride tetrahydrate	$MnCl_2•4H_2O$		
Hydrochloric acid	HCl		Sinopharm Chemical Reagent Co., Ltd.
Sodium hydroxide	NaOH		
Sodium nitrate	$NaNO_3$		
Humic acid	$C_9H_9NO_6$		
Methanol	CH_4O		
Anhydrous ethanol	C_2H_6O		
Tert-butanol	$C_4H_{10}O$		
L-histidine	$C_6H_9N_3O_3$		
Urea	CH_4N_2O		
Sodium chloride	NaCl		
Sodium bicarbonate	$NaHCO_3$		Nanjing Chemical Reagent Co., Ltd.
Potassium dihydrogen phosphate	KH_2PO_4		
P-benzoquinone	$C_6H_4O_2$		

2.2. Material characterization methods

Microstructural observation of gold-coated specimens was carried out using a Hitachi SU8020 instrument (Hitachi Corporation, Japan), with images obtained at various magnifications under accelerating voltages ranging from 0.1 to 30 kV. This allowed for detailed examination of the microstructure of the prepared materials, as well as analysis of their composition and structural features.

Phase identification of the prepared materials was performed via X-ray diffraction (XRD) using an X-7000 instrument (Shimadzu Corporation, Japan), which enabled the qualitative determination of phase constituents and elucidation of the crystal structure of simple crystals.

Fourier-transform infrared spectroscopy (FT-IR) was employed to identify functional groups and chemical bonds present in the catalyst, utilizing a Nicolet IS5 FT-IR spectrometer (Thermo Scientific, USA).

The specific surface area, pore size distribution, and pore volume of samples were evaluated through nitrogen adsorption-desorption measurements conducted on an Autosorb iQ2 BET analyzer (Kantar Instruments Inc., USA).

Surface analysis of solid material samples was conducted using an AXIS ULTRA DLD X-ray photoelectron spectrometer (Tsushima Kratos, Japan), which facilitated the investigation of elemental species, their chemical valence states, and their relative abundances on material surfaces.

2.3. Preparation of catalysts

For BC preparation, raw *A. calamus* material was cleaned with ultrapure water, cleaned leaves were placed in an oven for natural drying, and transferred to a high-speed crusher. Green *A. calamus* powder was obtained by passing through a 100-mesh sieve, wrapped in tin foil to create a limited oxygen environment, placed in a ceramic crucible, and calcined at high temperature in a muffle furnace. The temperature was increased to 600 ℃ at 5 ℃/min and held for 1.5 h. After cooling, the black BC powder was rinsed with anhydrous ethanol and ultrapure water to remove residual salts and organic matter, placed in an oven for natural drying, ground with a mortar, and stored after passing through a 100-mesh sieve.

Mn/N-BC was prepared by immersing 1 g of *A. calamus* powder in a mixed solution of $MnCl_2 \cdot 4H_2O$ and urea at different concentrations and sonicated for 30 min. After stirring at room temperature using a magnetic stirrer at 250 rpm for 24 h, the mixture was dried in a vacuum oven, and the resulting solid was ground and passed through a 100-mesh sieve. Next, the BC preparation procedure was replicated to produce seven distinct BC:N:Mn composites with mass ratios of 1:1:0, 1:0:1, 1:1:0.5, 1:0.5:1, 1:1:1.5, 1:2:1, and 1:3:1. Among them, the 1:1:0 and 1:0:1 ratios were named N-BC and Mn BC, respectively, while the rest were named Mn/N-BC.

A schematic illustration of the entire fabrication process is provided in Figure 1.

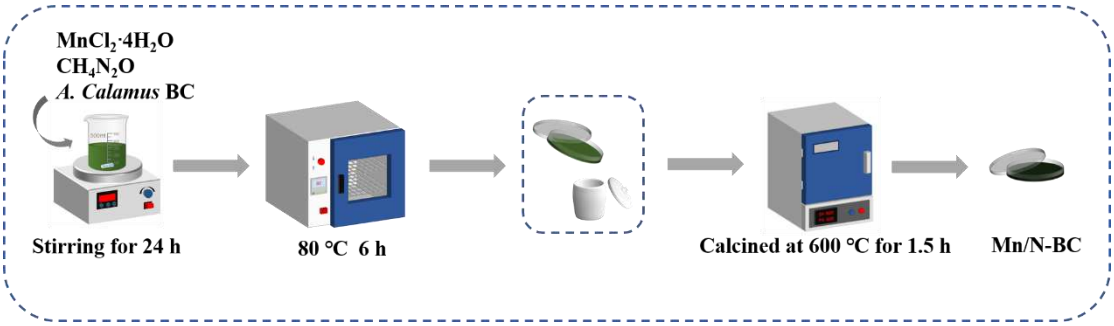

Fig. 1 The catalyst preparation process

2.4. Mn/N-BC adsorption degradation of TC

In adsorption experiments, 100 mL of TC solution (20 mg/L) was placed in a 200 mL beaker, and 1.0 g/L of Mn/N-BC powder was added and stirred at 150 rpm at room temperature. Samples were taken using a syringe at 0, 10, 20, 30, 45, 60, and 120 min and filtered through a 0.45 μm membrane to remove the catalyst powder.

In degradation experiments, adsorption was performed for 30 min as described above, and samples were removed to measure the TC concentration. $Na_2S_2O_8$ (2 mM) was immediately added to begin the degradation process. Samples were collected at time points identical to those for adsorption experiments. The aqueous samples, obtained by syringe, were filtered through a 0.45 μm membrane, after which the reaction was halted by addition of a small amount of methanol.

Three parallel experiments were set up for each group.

3. Results and Discussion

3.1. Characterization

3.1.1. Scanning electron microscopy (SEM) and energy-dispersive X-ray

spectroscopy (EDS)

SEM revealed morphological information for unmodified BC, Mn BC, N-BC, and Mn/N-BC materials (Figure 2). The original biochar has a rough sheet-like structure on its surface, which enhances its adsorption performance (Figure 2a). Figures 2b and 2c show images of carbon materials modified with Mn and N, respectively, which increases the surface roughness of the material and makes the layered structure more pronounced. The morphological characteristics of spherical Mn-N nanoparticles stacked on the layered structure of BC enable BC modified with Mn and N results in more active sites, which is beneficial for improving catalytic performance (Figure 2d).

Analyses of elemental composition and content were conducted by EDS and the results are shown in Figure 2e. Four elements, C, O, Mn, and N, were detected in the synthesized material. Among them, C and O account for a relatively large proportion among the four elements (65.37% and 29.45% respectively), with mass fractions of 44.18% and 17.52%, while Mn and N account for 11.43% and 3.75% respectively, with mass fractions of 35.35% and 2.95%.

Transmission electron microscopy (TEM) was performed the results analyzed by mapping MnN@BC to the element distribution of composite materials, with different colors representing successful loading of different elements onto BC (Figure 2f). The findings substantiate the efficacy of the proposed modification method, and reveal that the unique pore characteristics of the carbonized biomass are not compromised by calcination at 600 °C.

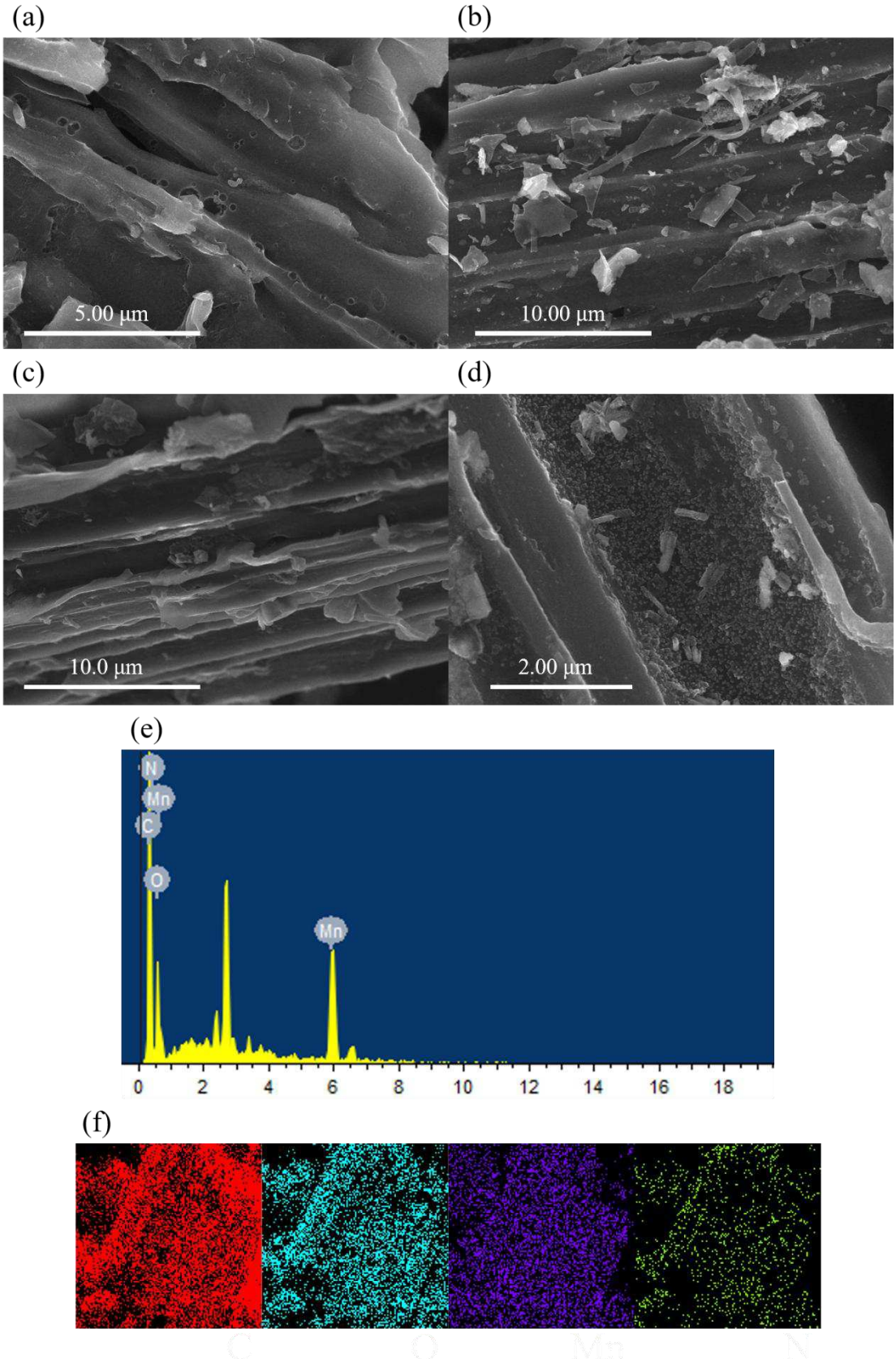

Fig. 2 SEM and TEM results. SEM images of (a) BC, (b) Mn-BC, (c) N-BC,

and (d) Mn/N-BC. (e) EDS spectrum and (f) TEM elemental mapping of Mn/N-BC

3.1.2. XRD analysis

As shown in Figure 3a, broad diffraction peaks were observed at 2θ = 23.25° and 43.24°, corresponding to amorphous and crystalline carbon in the (002) and (100) planes of BC [22, 23]. Compared with the original BC, the diffraction peak intensity of modified BC was significantly enhanced, and peak positions were shifted due to N doping. XRD spectra of Mn BC and Mn/N-BC show characteristic peaks at 2θ = 29.4° and 49.6°, corresponding to the (310) and (301) crystal planes of MnO_2 (JCPDS#72-1982), respectively. Peaks corresponding to MnO (JCPDS#77-2363) appear at 2θ = 41.4° and 73.0°, corresponding to the (200) and (222) crystal planes, respectively [24]. Characteristic peaks appearing at 2θ = 32.2° and 36.0° correspond to the (103) and (211) crystal planes of Mn_3O_4, respectively. These results indicate that there are characteristic peaks of manganese oxides with different valence states in materials co-doped with Mn and N, consistent with XPS data.

3.1.3. FT-IR analysis

Figure 3b shows FT-IR spectra obtained for BC, N-BC, Mn-BC and Mn/N-BC catalysts. The peak appearing at ~3413 cm^{-1} was attributed to O-H stretching vibrations, while asymmetric and symmetric stretching vibrations for C=O were also observed at 1607 cm^{-1}. The characteristic Mn-O peak was observed in spectra of Mn BC and Mn/N-BC at ~599 cm^{-1}, indicating the presence of manganese oxide. C-NH-C (1264 cm^{-1})

was also found in the Mn/N-BC spectrum. These results indicate that Mn and N were successfully loaded onto BC.

3.1.4. Brunauer-Emmett-Teller (BET) analysis

For deeper insight into how Mn and N modification alters the physical properties of the catalysts, BET analysis was performed on two BC variants, with their N_2 adsorption-desorption isotherms and Barrett-Joyner-Halenda (BJH) pore size distributions plotted accordingly. As shown in Figure 3c, the original BC and BC modified with Mn and N exhibit I and IV isotherms with H4 hysteresis loops, indicating the coexistence of micropores (<2 nm) and mesopores (2–50 nm) [25]. The pore size distribution curve in Figure 3d further supports this viewpoint. The BET surface area of BC loaded with Mn/N decreased significantly, from 117.534 m^2/g for original BC to 7.232 m^2/g, which may be due to the partial filling of pores caused by N doping [26]. Relative to BC, the Mn/N-BC sample has a reduced pore volume, a phenomenon probably linked to the dispersion of Mn particles within both micropores and mesopores [27], consistent with the decrease in Mn/N-BC adsorption performance. Such a layered porous morphology promotes catalytic activity via enhanced pollutant mass transfer kinetics [28].

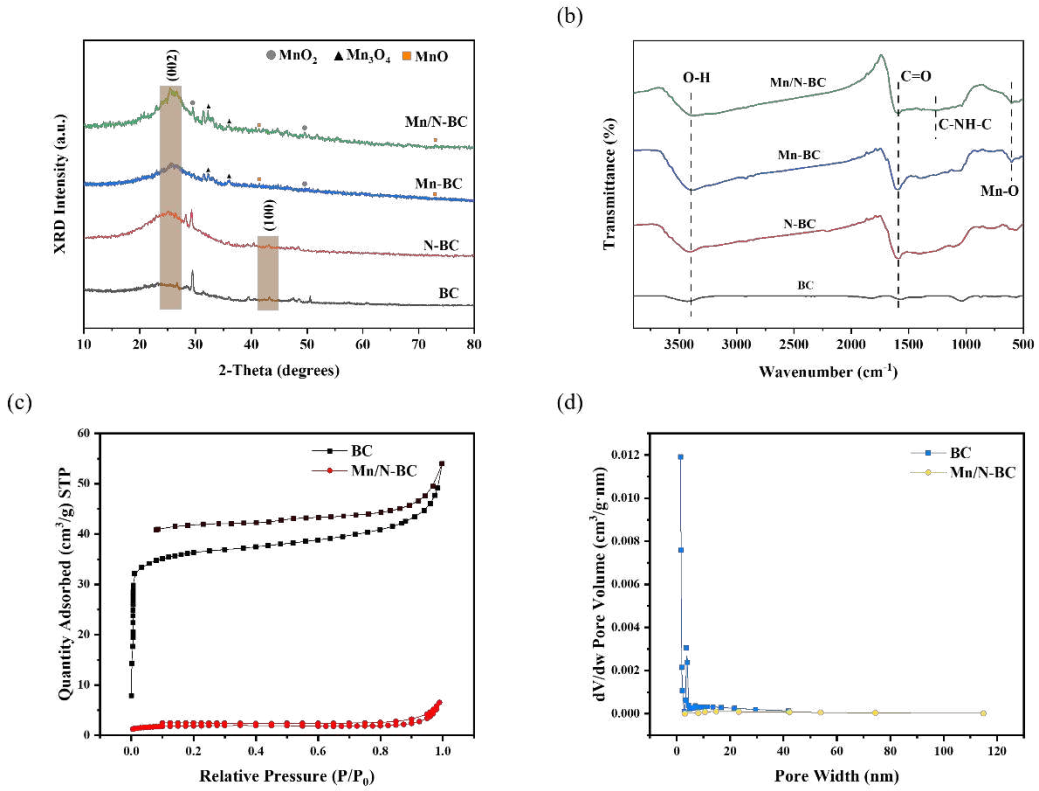

Fig. 3 Spectroscopic analyses of modified BC samples. (a) XRD patterns and (b) FT-IR spectra of BC, N-BC, Mn-BC, and Mn/N-BC. (c) N_2 adsorption desorption curves and (d) BJH aperture distribution map of BC and Mn/N-BC

3.1.5. XPS analysis

To investigate the chemical states of C, O, N, and Mn, XPS analysis was conducted on the Mn/N-BC catalyst both prior to and following reaction under optimized experimental conditions. The overall spectrum of the material and detailed spectra for each element are shown in Figure 4a–i. Due to consumption during the reaction, the characteristic Mn2p peak of the material is not significant after the reaction.

Figures 4b and c show C 1s fine spectra. The main peak at 284.57 eV is assigned to C-C, the peak at 287.22 eV is attributed to O-C=O, and the peak at 283.30 eV may

be ascribed to the interaction between carbon and manganese (C–Mn) or to defective carbon.

The O 1s spectra (Figures 4d and e) are fitted into three peaks. The peak at the lowest binding energy of 530.57 eV is characteristic of lattice oxygen (Mn-O) in manganese oxides, confirming the successful formation of MnO_x species as also detected by XRD . The peaks at 532.15 eV and 533.48 eV are assigned to surface oxygen vacancies and O-C=O groups, respectively.

Figures 4f and g show N 1s fine spectra, with pyridine N, pyrrole N, and graphite N detected at binding energies of 398.10 eV, 399.29 eV, and 400.20 eV, respectively [26]. The proportions of the three different types of N before the reaction were 52.58%, 24.51%, and 22.91%, respectively, among which pyridine N was the major form. However, after catalytic degradation, the content of graphitic N decreased to 11.91%. Therefore, as an additional active site for PDS activation, this result is consistent with previous research [29].

As shown in Figures 4h and i, the Mn 2p spectra feature peaks at binding energies of 640.75 eV, 642.27 eV, and 652.87 eV, which can be attributed to Mn(II), Mn(III), and Mn(IV) based on previous reports [30]. Specifically, the peak at ~640.75 eV is ascribed to Mn_2O_3, while the signal near 652.87 eV corresponds to MnO_2 [31, 32]. The proportions of Mn (II) and Mn (III) decreased from 44.31% and 30.75% before reaction to 39.75% and 23.72% after reaction, respectively. Upon completion of the reaction, the amount of Mn(IV) present in the catalyst was 36.52%. This is because divalent and trivalent Mn ions, as well as persulfate ions in PDS, form free radicals and complete

the process of transitioning to higher valence states.

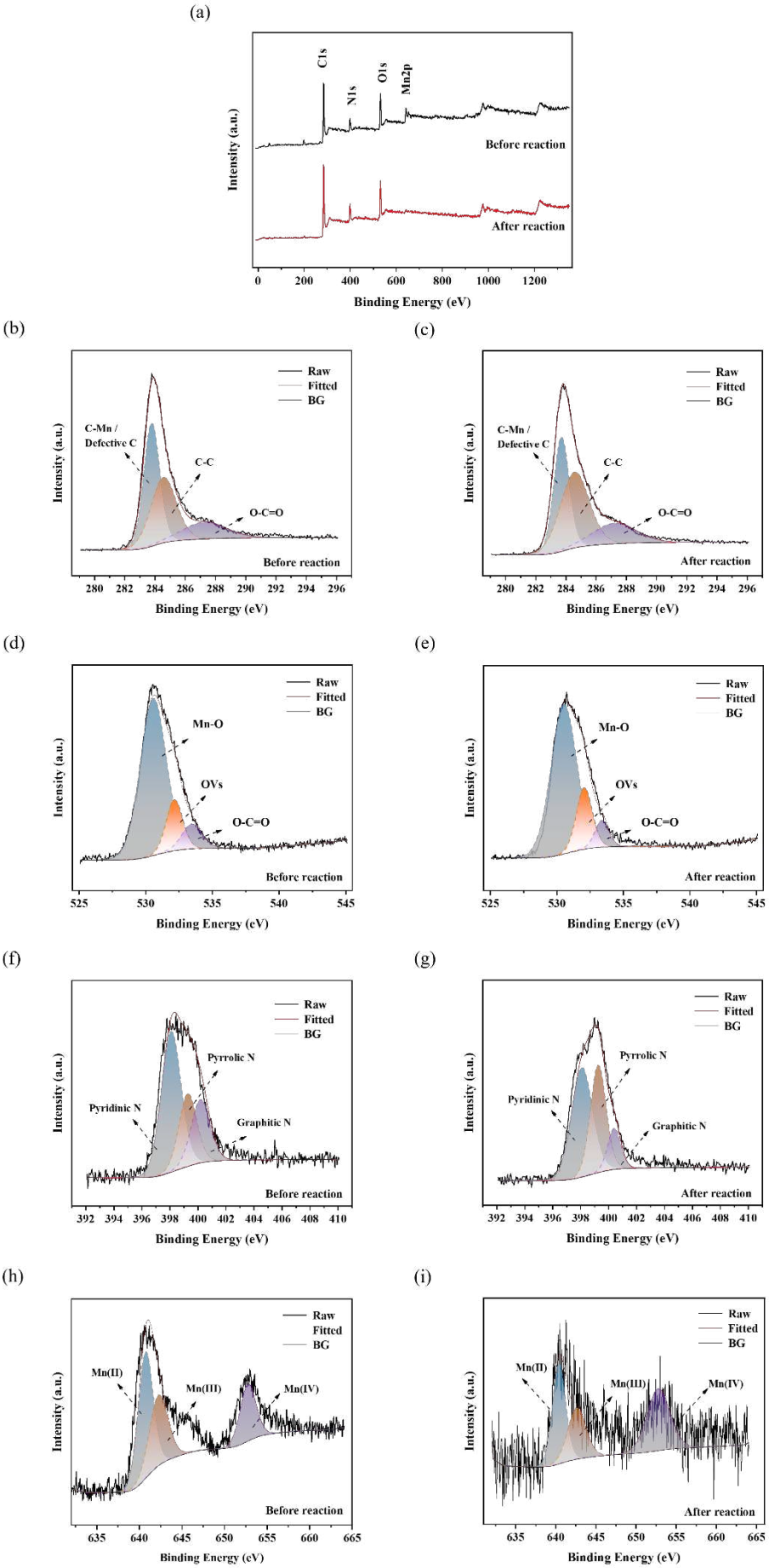
(a)
C1s
N1s
O1s
Mn2p
Before reaction
After reaction
Intensity (a.u.)
Binding Energy (eV)
(b)
(c)
Raw
Fitted
BG
C-Mn / Defective C
C-C
O-C=O
Before reaction
After reaction
(d)
(e)
Mn-O
OVs
(f)
(g)
Pyrrolic N
Pyridinic N
Graphitic N
(h)
(i)
Mn(II)
Mn(III)
Mn(IV)

Fig. 4 XPS analysis of modified BC samples. XPS spectra of (a) Mn/N-BC, (b-c) C 1s, (d and e) O 1s, (f and g) N 1s, and (h and i) Mn 2p

3.2. Performance of Mn/N-BC degradation of TC

In order to investigate the optimal ratio of BC, N, and Mn, six different catalyst ratios were tested: BC:N:Mn = 1:0:1, 1:1:0.5, 1:0.5:1, 1:1:1.5, 1:2:1, and 1:3:1. Adsorption-degradation experiments were carried out under optimal conditions, and the TC removal efficiency is presented in Figures 5a and b. When the doping ratio of BC to N was the same (1:1), as the Mn doping content increased, the TC removal rate exhibited a corresponding rise from 60.09% to 93.76%. However, as the doping amount continued to increase, the removal rate of TC slightly decreased. As the doping amount of N element increased, the removal effect of TC gradually decreased, which may be because a large amount of urea had not completely altered the internal structure of BC. However, a portion of N elements adhered to the surface of BC, decreasing the available active sites on the material surface and affecting PDS activation, thereby lowering the removal efficiency. It can therefore be concluded that the optimal doping ratio of BC, N, and Mn is 1:1:1.

To evaluate material performance, a series of adsorption and degradation experiments were implemented under varying experimental systems. The experiment was divided into nine groups, with PDS acting alone on four materials: TC and BC, Mn BC, N-BC, and Mn/N-BC. Experiments were conducted with a catalyst dosage of 1.0 g/L, 2 mM PDS, and 20 mg/L TC. The results are shown in Figures 5c and d. Adding

only PDS had almost no effect on TC degradation. When only BC was present for adsorption, the TC removal rate reached 48.52%. After doping with different heteroatoms, the TC removal rate decreased from approximately 4.18% to 11.83%, indicating a decrease in the adsorption performance of the material, consistent with the results of BET specific surface area measurement. This may be because metal particles occupy the surface and porous structure of BC. The catalyst effectively activated PDS to produce reactive free radicals, resulting in a significantly higher TC degradation rate than that achieved in the absence of PDS. The removal rates of Mn BC+PDS, N-BC+PDS, and Mn/N-BC+PDS groups were 68.00%, 60.65%, and 93.76%, respectively. The effect of metal non-metal co-doping was particularly significant, and the reaction rate was fast, reaching 0.0199 min^{-1}.

Under different experimental conditions (PDS/PMS concentration, catalyst loading), direct comparisons are relatively complex, yet the present system offers several distinct advantages. The MnN@BC material developed by Liu et al. [33] was applied in a more energy-intensive three-dimensional electro-activation system, whereas the Mn/N-BC in this study achieved comparably high performance through simple catalyst addition, demonstrating its superior energy efficiency. Under the optimal conditions of 1.0 g/L catalyst, 2 mM PDS, and 20 mg/L TC, the TC removal rate reached 93.76% with a rate constant of 0.0199 min^{-1}, surpassing the δ-MnO_2/BC+PS system (85.5%) [34].

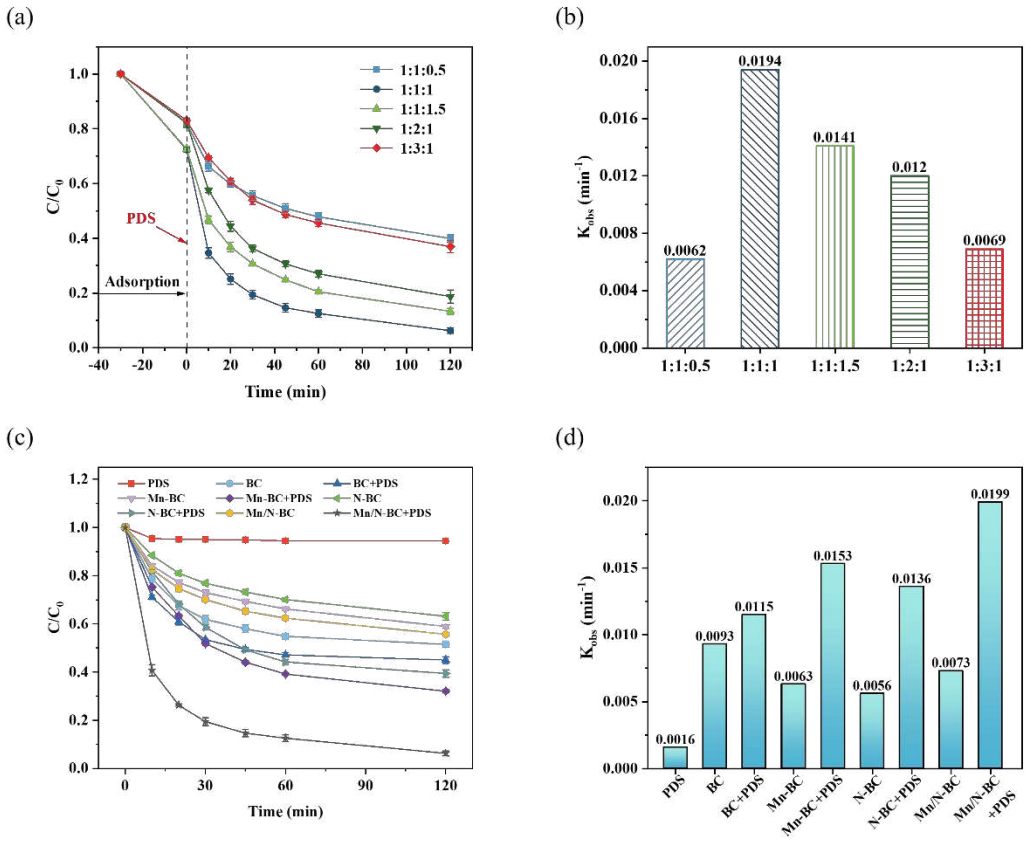

Fig. 5 Mn/N-BC degradation of TC. (a) Degradation of TC by mass ratio of BC, N, and Mn and (b) pseudo first order rate constant. (c) Catalytic degradation experiments for different systems and (d) pseudo first order rate constant

3.3. Factors influencing reaction rates

3.3.1. PDS dosage

The use of persulfate in advanced oxidation for water remediation inevitably generates sulfate ions, which can cause corrosion in wastewater systems. Therefore, it is extremely important to investigate the dosage of PDS [35]. Figure 6a shows that the removal efficiency of TC rose steadily as the concentration of PDS was increased. When the PDS concentration was 0.5 and 1.0 mM, only 72.82% and 86.72% of TC was removed, respectively. A further rise in concentration did not yield continued

enhancement in TC removal, with the degradation rate stabilizing at ~93.76%. One explanation is that when the amount of catalyst added in the reaction system is fixed, the number of electrons generated is limited, and excessive PDS will undergo self-quenching reaction with the generated $SO_4^{\bullet -}$ radicals, resulting in a decrease in active species in the reaction system.

3.3.2. Mn/N-BC dosage

The amount of material added is also an important influencing factor. Therefore, this experiment studied the degradation effect of TC at Mn/N-BC dosages of 0.3, 0.5, 0.7, 1.0, and 2.0 g/L. As shown in Figure 6b, during the adsorption stage, with an increase in catalyst content, the adsorption performance of the material for pollutants in water gradually increased, from 12.22% at a dosage of 0.3 g/L to 37.19% at a dosage of 2.0 g/L. It can be inferred from these data that, up to a certain point, elevating the catalyst dosage leads to enhanced pollutant adsorption. Within the catalytic degradation stage, an increase in BC dosage from 0.05 g/L to 0.1 g/L led to optimal TC removal of 93.76%, and notably fast degradation kinetics. However, when the dosage of Mn/N-BC was increased further to 2.0 g/L, the removal rate did not show a significant increase, which may be due to competition with pollutants for $SO_4^{\bullet -}$ when excessive metal and non-metal elements were co-doped [36].

3.3.3. Initial TC concentration

Figure 6c provides a visual representation of the relationship between initial TC

concentration and removal efficiency. The experimental results show that the adsorption effect of TC at low concentrations (10 and 20 mg/L) was strong, reaching 28.52%. As the concentration of pollutants increased, the adsorption effect gradually decreased to 17.64%. In the degradation experiment, the low concentration TC solution had the highest degradation efficiency (>93.00%) and the fastest degradation rate. With gradually increasing TC concentration, both the degradation rate and the resulting removal efficiency diminished. These results imply that due to restricted adsorption capacity, degradation intermediates compete alongside TC for radical species, contributing to the observed decline in removal performance. From this, it can be concluded that construction of a Mn/N-BC+PDS catalytic system has broad application prospects for treating wastewater containing pollutants at different concentrations.

3.3.4. Initial pH value

Sewage from different sources can differ in terms of pH. The effects of initial solution pH on pollutant removal efficiency were investigated using NaOH and HCl to adjust pH. Previous studies have shown that PS can be efficiently activated over a wide pH range [25], and our experimental results supported this conclusion. As shown in Figure 6d, the TC removal rate remained at ~93.00% across a pH of 3–9, and the reaction rate constant remained relatively high (~0.0190 min^{-1}). A further rise in pH to 11 resulted in a diminished degradation efficiency of 74.89% and a marked decrease in reaction rate. This indicates that alkaline conditions can limit PDS activation (i.e. PDS may decompose in alkaline solutions) [37]. These results indicate that within the Mn/N-

BC/PDS system for wastewater treatment, an acidic environment is usually advantageous for pollutant breakdown. Therefore, the removal efficiency of pollutants can be optimized by adjusting the pH value of sewage. Acidic conditions have broader application prospects for treatment of sewage with different pH values.

3.3.5. Inorganic anions and humic acids

Common inorganic anions (such as Cl^-, HCO_3^-, $H_2PO_4^-$, and NO_3^-) and humic acid (HA) can significantly affect the removal of pollutants in a system [38]. Therefore, the removal efficiency of TC was studied at different concentrations of inorganic anions (5, 10, and 20 mM). According to Figure 6e, $H_2PO_4^-$ and NO_3^- exerted negligible effects on the catalytic adsorption-degradation process, indicating minimal interference. However, upon addition of Cl^-, decomposition of TC was enhanced in the Mn/N-BC+PDS system. At Cl^- concentrations of 5, 10, and 20 mM, the degradation rate of TC reached 95.59%. Research has shown that the Cl^- reaction can generate ClO^-, which rapidly oxidizes pollutants [39]. In contrast, HCO_3^- impeded TC removal, and this inhibitory effect was amplified with increasing concentration of the anion. As the concentration of HCO_3^- increased, the TC removal rate decreased to 70.32%, which may be due to HCO_3^- scavenging $SO_4^{\bullet-}$ and •OH, thereby inhibiting the degradation of TC [33]. In addition, both HCO_3^- and PDS carry negative charges, leading to adsorption competition and affecting PDS activation.

Figure 6f illustrates the impact of HA on the degradation of TC. With an increase in HA concentration from 5 mM to 20 mM, the adsorption and degradation performance

of the Mn/N-BC+PDS system was improved. Higher HA concentrations led to an increasingly pronounced suppression of TC removal. This may be due to competition between HA and pollutants for adsorption sites, which in turn affects their adsorption and degradation efficiency. Additionally, the active sites are occupied, which affects activation of PDS by the catalyst.

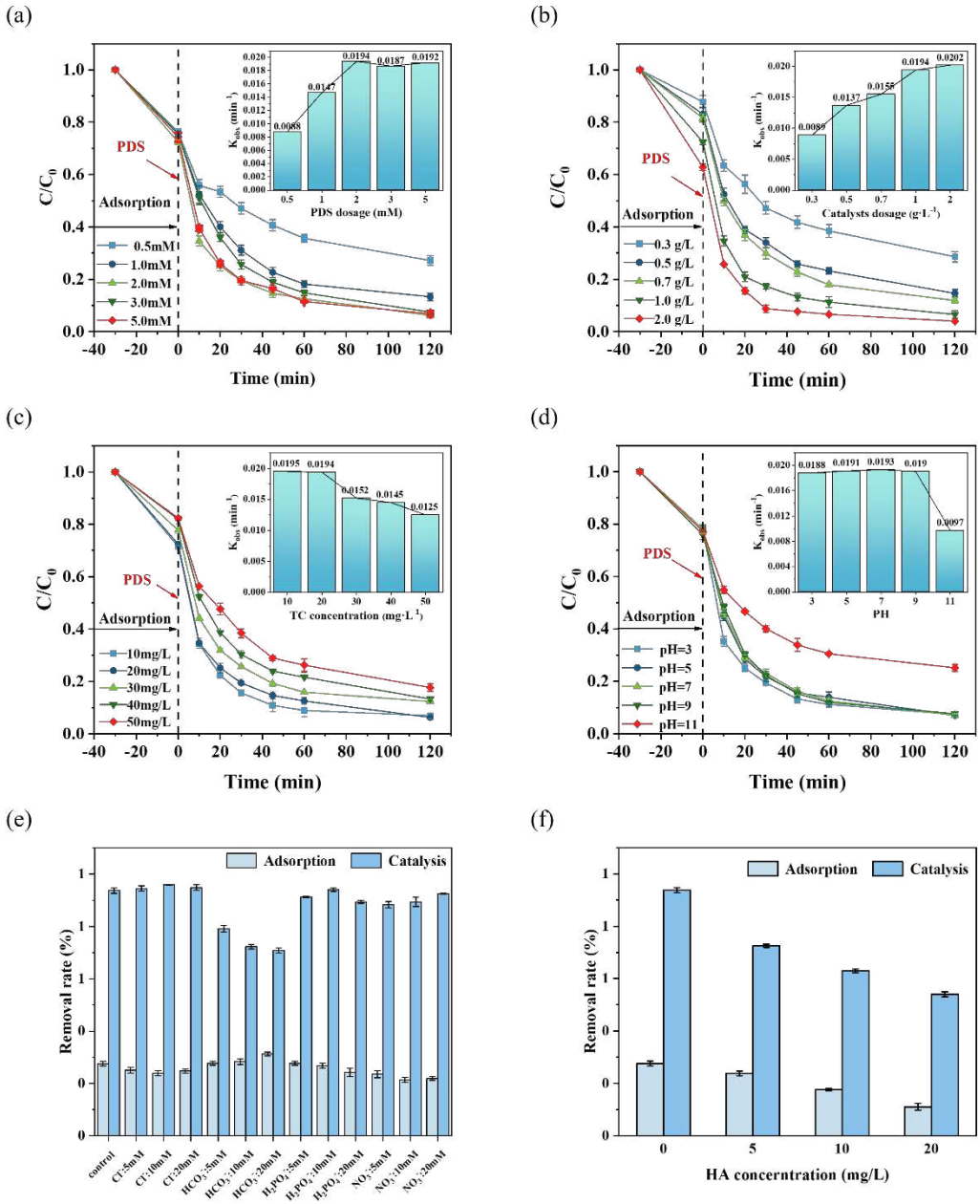

Fig. 6 Analysis of factors influencing reaction rates. Effects of (a) PDS concentration, (b) Mn/N-BC dosage, (c) initial TC concentration, (d) pH value, (e)

different concentrations of inorganic anions, and (f) different concentrations of HA on TC degradation

3.4. Cycle stability and dynamic analyses

In order to explore the preliminary feasibility of the Mn/N-BC+PDS system, cyclic stability experiments were conducted to ensure that the initial conditions for each experiment were identical (i.e., consistent with the TC degradation experiment). This experiment serves as a proof-of-concept to evaluate catalyst retention and short-term performance under dynamic conditions, rather than a fully optimized engineering demonstration. As shown in Figure 7a, the Mn/N-BC catalyst achieved TC degradation of 93.8%, 86.0%, and 80.3% after one, two, and three cycles, respectively. The gradual decline in efficiency may be attributed to the potential leaching of Mn active centers, which is commonly observed in metal–carbon composite catalysts. The Mn/N-BC catalyst retained more than 80% of its initial activity after three consecutive cycles, demonstrating favorable short-term reusability.

To demonstrate the potential for laboratory-scale application, we will ensure that further studies are carried out under more practical continuous-flow conditions. Figure 7b presents a schematic diagram of the experimental configuration, which includes a peristaltic pump (power unit), a beaker (storage tank), and a reaction column. Quartz sand was placed at the inlet and outlet of the reaction column to prevent catalyst powder from escaping with the water flow, and several pieces of polyurethane sponge (3 cm × 3 cm × 3 cm) loaded with 0.1g Mn/N-BC powder were included. The dynamic

experiment was carried out under stable room temperature conditions. A peristaltic pump was used to continuously feed a mixed solution containing PDS (2 mM) and TC (20 mg/L) into the reaction column, with effluent samples collected every 30 min for TC concentration analysis. To account for the adsorptive capacity of quartz sand, an unfilled catalyst was used as a reference control. The experimental results are shown in Figure 7c. The TC removal rate decreased from 83.1% to 69.0%.

(a)

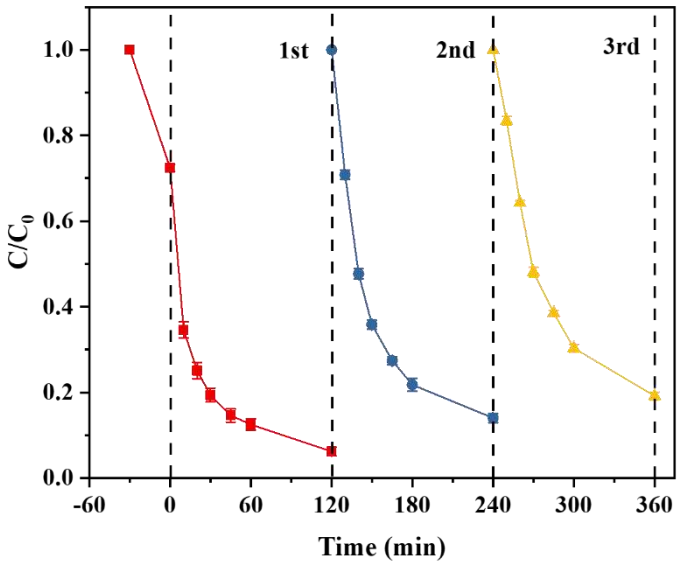
1st
2nd
3rd
C/C0
Time (min)

(b)

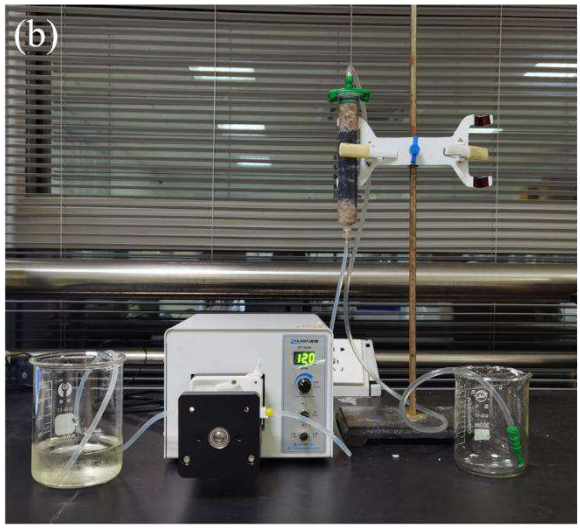

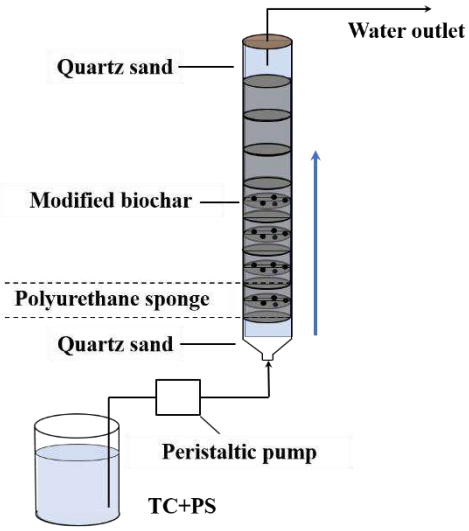
Water outlet
Quartz sand
Modified biochar
Polyurethane sponge
Quartz sand
Peristaltic pump
TC+PS

(c)

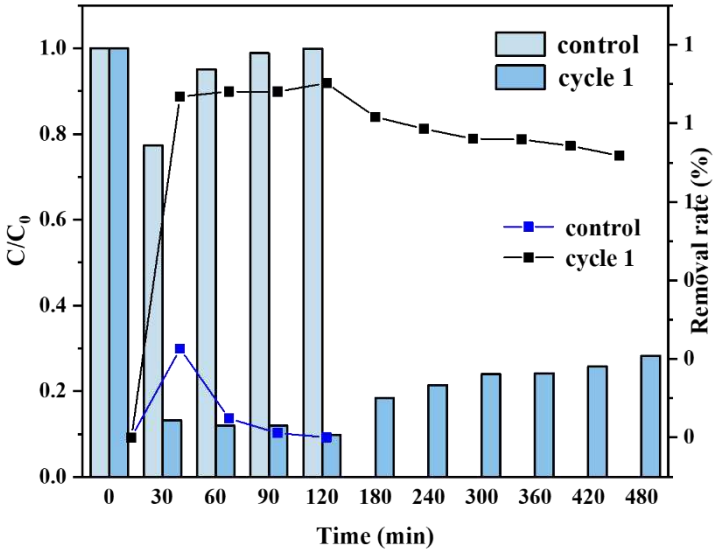
control
cycle 1
control
cycle 1
C/C0
Removal rate (%)
Time (min)

Fig. 7 Cycle stability and dynamic analyses. (a) Cycle results for Mn/N-BC degradation of TC. (b) Schematic diagram of the dynamic experimental column. (c) Dynamic degradation of TC in the Mn/N-BC system

3.5. Degradation mechanism analysis

3.5.1. Identification of active species and EPR analysis

Electron paramagnetic resonance spectroscopy (EPR) was employed for qualitative analysis of active substances. Two spin capture agents, 5,5-Dimethyl-1-pyrrolineN-oxide (DMPO) and 2,2,6,6-Tetramethylpiperidinooxy (TEMP), were used to capture $SO_4^{\bullet-}$, •OH, and $^1O_2$. Free radicals and non-free radicals were captured at 0 min and 10 min, respectively. The results are shown in Figures 8a and b. After 10 min of reaction, characteristic 1:2:2:1 and 1:1:1:1:1 signal peaks were observed, respectively corresponding to •OH and $SO_4^{\bullet-}$ [40]. In addition, a characteristic 1:1:1 peak was detected, indicating the production of $^1O_2$ during the catalytic degradation of pollutants. In summary, three active substances were co-captured by EPR, namely $SO_4^{\bullet-}$, •OH, and $^1O_2$, and they participate in the degradation of TC.

The reactive species generated during TC degradation by the Mn/N-BC+PDS system were identified through radical quenching tests and EPR analysis. MeOH, TBA, L-His, and P-BQ were selected as active substance quenchers, while a group without quenchers served as a blank control. The reaction rates of MeOH with free radicals $SO_4^{\bullet-}$ and •OH were 2.5×10^8 $M^{-1}\cdot s^{-1}$ and 9.7×10^8 $M^{-1}\cdot s^{-1}$, respectively [41], making them a scavengers of $SO_4^{\bullet-}$ and •OH. Due to the higher reaction rate between TBA and

•OH compared to $SO_4^{\bullet-}$ ($k_{\bullet OH} = 3.8–7.6\times10^8\ M^{-1}\cdot s^{-1} > k_{SO_4^{\bullet-}} = 4.0–9.1\times10^5\ M^{-1}\cdot s^{-1}$) [42], it is only used for scavenging •OH; L-His and P-BQ respectively quench non-free radical $^1O_2$ ($k_{^1O_2} = 3.2\times10^8\ M^{-1}\cdot s^{-1}$) and radical $O_2^{\bullet-}$ ($k_{O_2^{\bullet-}} = 9.0\times10^8\ M^{-1}\cdot s^{-1}$) [43]. The experimental results are shown in Figures 8c and d. Addition of P-BQ had a strong inhibitory effect, reducing the TC removal rate to 55.6%. Both groups with added MeOH and L-His displayed certain inhibitory effects, with TC removal rates of 73.3% and 75.1%, respectively. The inhibitory effect of TBA on TC removal was weakest, at 81.8%.

The contribution rates of various reactive species to TC degradation were calculated as described previously (Equations 1-4) [44]. According to kinetic calculations, the contribution rates were ordered (from high to low) $O_2^{\bullet-}$, $^1O_2$, •OH, and $SO_4^{\bullet-}$, and 73.7% >51.5% >39.2% >13.4%. Therefore, it can be inferred that all four reactive species are involved in PDS activation, with $O_2^{\bullet-}$ and $^1O_2$ serving as the predominant contributors.

$$\bullet OH: \left(K_{control}-K_{TBA}\right)/K_{control} \quad (1)$$

$$SO_4^{\bullet-}: \left(K_{TBA}-K_{MeOH}\right)/K_{control} \quad (2)$$

$$^1O_2: \left(K_{control}-K_{L\text{-}His}\right)/K_{control} \quad (3)$$

$$O_2^{\bullet-}: \left(K_{control}-K_{P\text{-}BQ}\right)/K_{control} \quad (4)$$

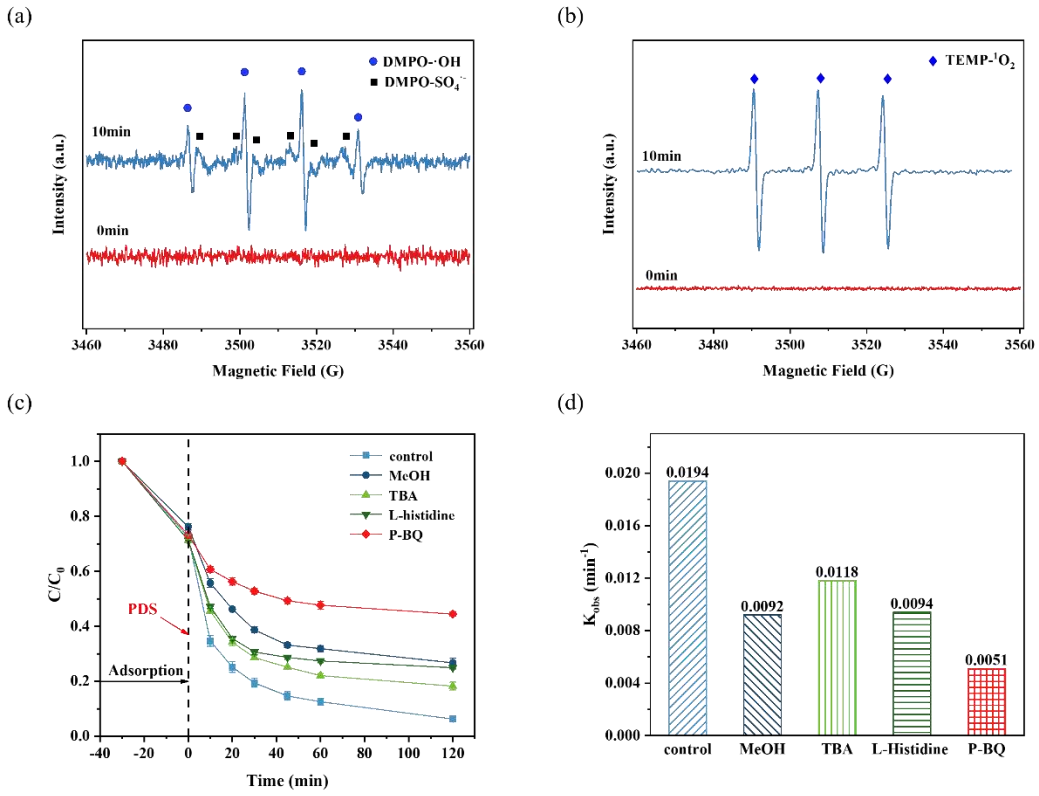

Fig. 8 EPR analysis of TC degradation. EPR spectra of (a) $SO_4^{\bullet-}$ and •OH, and (b) $^1O_2$. (c) Effects of different quenching agents on TC degradation and (d) pseudo first order rate constant

3.5.2. Reaction mechanism

By combining XPS before and after the reaction, changes in different chemical bonds and metal ion valence state contents were analyzed to probe the degradation mechanism of TC in the Mn/N-BC+PDS system (Figure 9a). Free radical quenching experiments and EPR characterization were combined to analyze the active substances involved in the degradation process. Compared with Mn doping, co-doping of Mn and N can fix more Mn atoms on the catalyst surface. A large amount of Mn (II) and Mn (III) provide more electrons, causing PDS to decompose and generating free radicals

(Equations 5 and 6). Peroxysulfates and the free radicals generated by their activation convert into the other two types of free radicals in water (Equations 7 and 8). Studies have shown that $^1O_2$ is the main non-free radical, which can be generated by the ketone carbonyl group C=O at the edge of the C-complex on N-doped BC [45]. In addition, N doping leads to many structural defects that can activate PDS and generate free radicals. Defective structures can also promote electron transfer and improve the performance of catalysts. The observed decrease in C=O content (from 15.8% to 14.2%) means that the C=O group is consumed in the reaction. Meanwhile, trace amounts of $^1O_2$ can also be generated (Equation 9) [46].

$$Mn\ (II) + S_2O_8^{2-} \rightarrow Mn\ (III) + SO_4^{2-} + SO_4^{\bullet-} \quad (5)$$

$$Mn\ (III) + S_2O_8^{2-} \rightarrow Mn\ (IV) + SO_4^{2-} + SO_4^{\bullet-} \quad (6)$$

$$SO_4^{\bullet-} + H_2O \rightarrow \bullet OH + SO_4^{2-} + H^+ \quad (7)$$

$$3S_2O_8^{2-} + 4OH^- \rightarrow 6SO_4^{2-} + 2O_2^{\bullet-} + 4H^+ \quad (8)$$

$$2O_2^{\bullet-} + 2H_2O \rightarrow {}^1O_2 + H_2O_2 + 2OH^- \quad (9)$$

3.5.3. Degradation pathway analysis

By integrating the results of radical characterization with the intermediate products detected in liquid chromatography-mass spectrometry (LC-MS) experiments (Table 2), three plausible degradation pathways were deduced.

Table 2 Structural information for intermediates products detected by LC-MS

Serial number	Mass-to-charge	Molecular	Structural formula

	ratio (m/z)	formula	
P0	445	$C_{22}H_{24}N_2O_8$	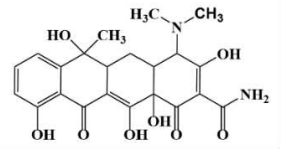
P1	430	$C_{21}H_{22}N_2O_8$	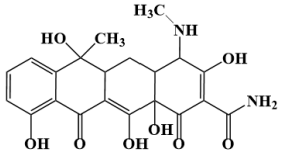
P2	346	$C_{19}H_{22}O_6$	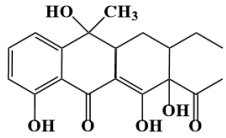
P3	302	$C_{17}H_{18}O_5$	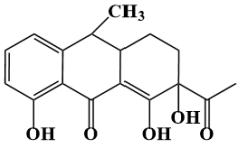
P4	396	$C_{21}H_{21}NO_7$	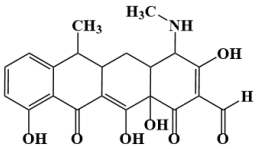
P5	274	$C_{16}H_{18}O_4$	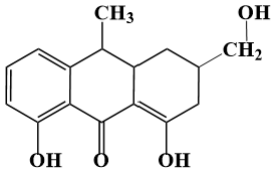
P6	136	$C_8H_8O_2$	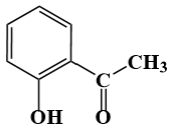
P7	122	$C_8H_{10}O$	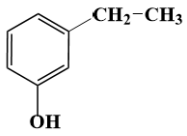
P8	60	$C_2H_4O_2$	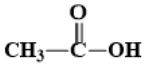
P9	461	$C_{22}H_{26}N_2O_9$	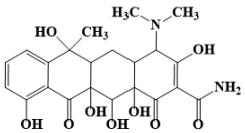

P10	432	$C_{21}H_{23}NO_9$	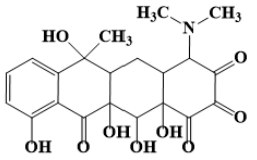
P11	349	$C_{18}H_{22}O_7$	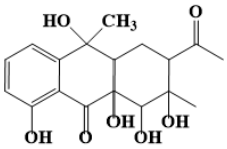
P12	305	$C_{16}H_{18}O_6$	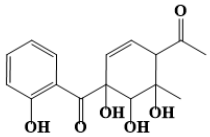

Studies have shown that electron donor groups and ionizable groups (such as dimethylamine, amide, and double bonds) are susceptible to reactive free radical attack, leading to TC decomposition [47]. The present work proposes three possible degradation pathways for TC, as shown in Figure 9b. It should be noted that due to the complexity of radical chain reactions, other minor pathways or isomers may also exist. In pathway one, the amino group is readily attacked by $O_2\bullet^-$, resulting in deamination to form P1 (m/z = 429). Next, through dehydroxylation, demethylation, and loss of methylamine groups, P2 (m/z = 346) is formed, which is further degraded to generate P3 (m/z = 302) via continuous oxidation [48]. In pathway two, the hydroxyl groups, water molecules, and amino groups on P0 are first removed, yielding P4 (m/z = 396). The intermediate product P5 (m/z = 274) is obtained through ring cleavage, and finally converted to P6 (m/z = 136), P7 (m/z = 122), and P8 (m/z = 60) through ring opening reaction [49]. In pathway three, reactive oxygen species ($O_2\bullet^-$ and $^1O_2$) attack TC and form hydroxylation product P9 (m/z = 461). Subsequent reactions involving deamination, cleavage of the C=C bond, and further oxidation convert compound P9

into compound P10 (m/z = 432) . The cyclic ketone structure is subsequently oxidized and opened to form compound P11 (m/z = 349). As the degradation reaction proceeds, further oxidative decomposition and ring opening reactions occur, producing intermediate product P12 (m/z = 305) [50].

(a)

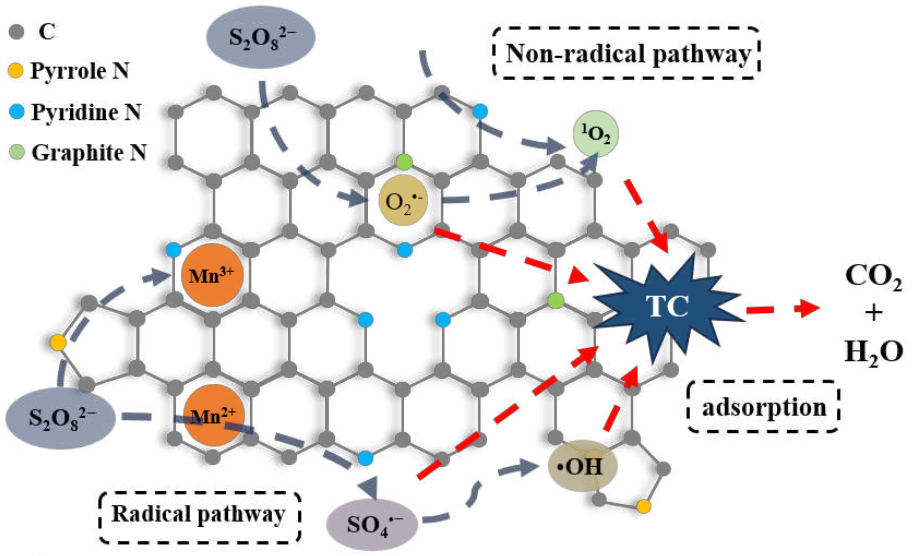
C
Pyrrole N
Pyridine N
Graphite N
$S_2O_8^{2-}$
Non-radical pathway
$^1O_2$
$O_2^{\bullet-}$
Mn^{3+}
TC
CO_2 + H_2O
adsorption
$S_2O_8^{2-}$
Mn^{2+}
•OH
Radical pathway
$SO_4^{\bullet-}$

(b)

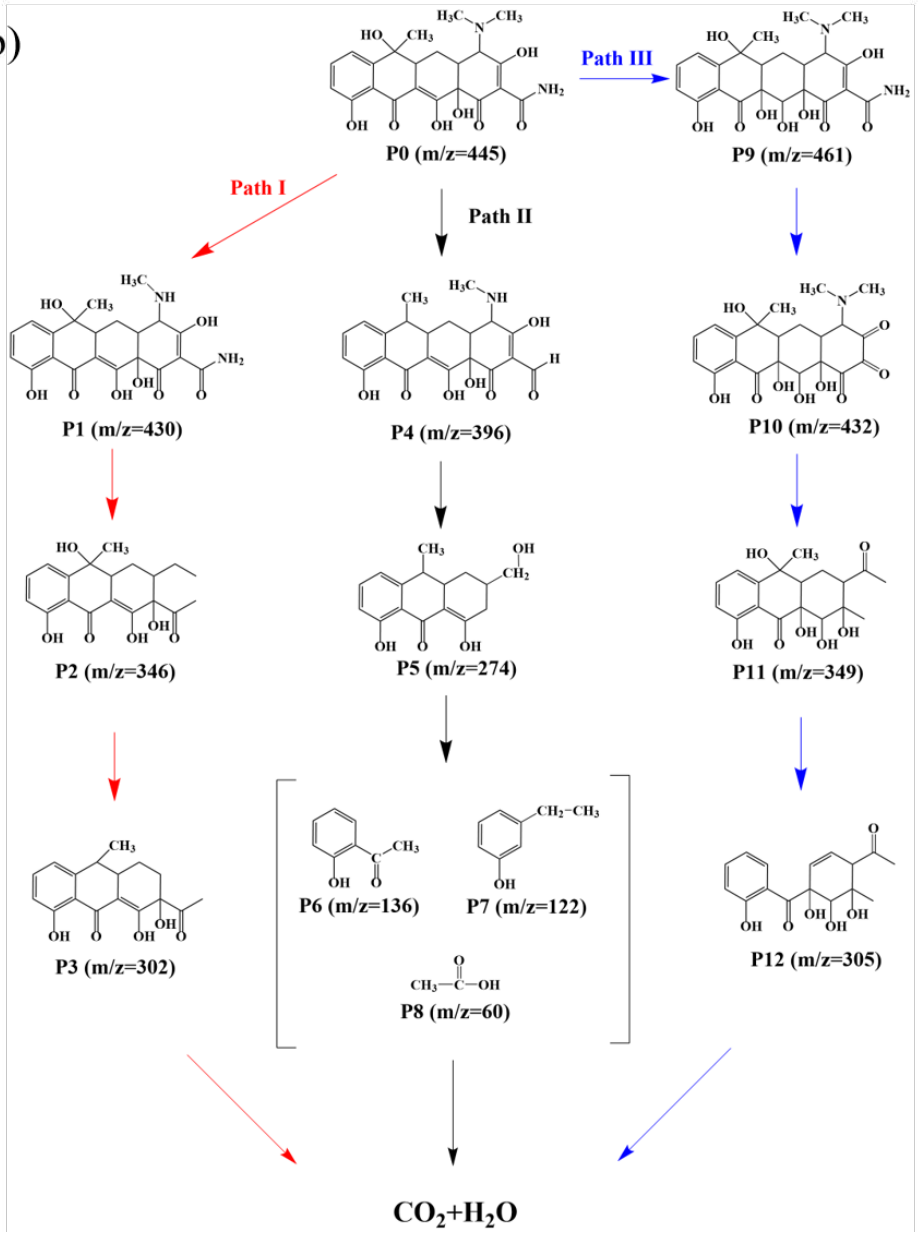
P0 (m/z=445)
Path III
P9 (m/z=461)
Path I
Path II
P1 (m/z=430)
P4 (m/z=396)
P10 (m/z=432)
P2 (m/z=346)
P5 (m/z=274)
P11 (m/z=349)
P6 (m/z=136)
P7 (m/z=122)
P3 (m/z=302)
P12 (m/z=305)
P8 (m/z=60)
CO_2+H_2O

Fig. 9 (a) **TC degradation reaction mechanism.** (a) Mechanism diagram of TC degradation by the Mn/N-BC+PDS system. (b) TC degradation pathways in the Mn/N-BC+PDS system

3.6. Toxicity testing

The ecological toxicity of TC and its intermediates (P0–P12) was analyzed using the toxicity assessment software tool (TEST), and the acute toxicity of TC was evaluated using the lethal concentration killing 50% of test animals (LC_{50}) against *Fathead minnow* and water flea (*Daphnia magna*). It is crucial to emphasize that these are computational predictions, not experimental bioassays. These values were 0.90 mg/L and 5.44 mg/L, respectively (Figures 10a and b), consistent with previous studies [51]. This confirms that TC is a toxic organic pollutant. The LC_{50} values of intermediates P6–P12 for TC degradation in *Fathead minnow* indicate low toxicity (Figure 10a). All intermediate products except for P4 exhibited LC_{50} values greater than that of TC against water fleas (Figure 10b). These results indicate that TC degradation leads to a decrease in the toxicity of intermediates, but some intermediates retain high toxicity.

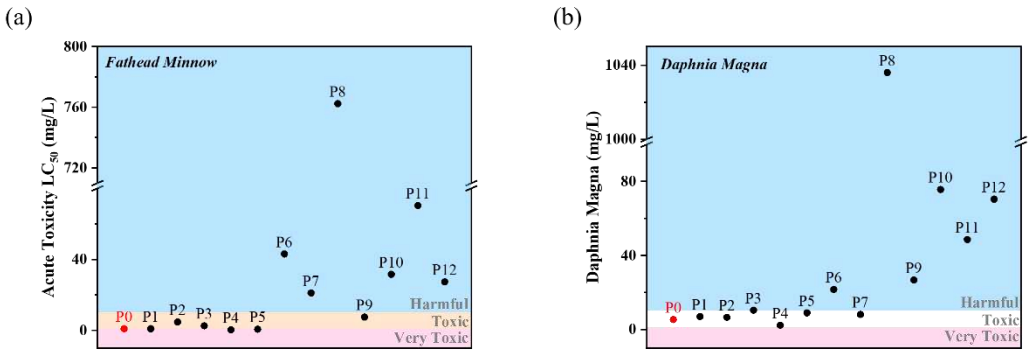

Figure. 10 Toxicity analysis. Acute toxicity of TC degradation intermediates evaluated by TEST against (a) *Fathead minnow* and (b) *Daphnia magna*

4. Conclusion

This work investigated the degradation performance and reaction mechanism of a Mn/N-BC-activated PDS system prepared using Mn/N-BC catalyst from *A. calamus* as raw material, against TC as a target pollutant. XRD and XPS analyses revealed nitrogen in the form of pyridine N, pyrrole N, and graphite N, and manganese in the form of Mn (II) and Mn (III). Co-doping of these two elements provides a large number of surface active sites for PDS activation. Under optimal experimental conditions (2 mM PDS, catalyst dosage 1.0 g/L, TC concentration 20 mg/L, pH 7) and the optimal doping ratio of BC:N:Mn = 1:1:1, the system achieved a TC removal rate of 93.67% within 120 min, mainly through two pathways involving free radicals (SO_4•$^-$, •OH, O_2•$^-$) and non-free radicals ($^1O_2$), among which O_2•$^-$ and $^1O_2$ play a dominant role. Based on LC-MS identification of 12 reaction intermediates, three plausible pathways for the degradation process are proposed. Additionally, the TC solution treated with Mn/N-BC was toxic; despite the reduced toxicity, a small quantity of highly toxic intermediates persisted.

Acknowledgments

The authors express their sincere gratitude to the National Key Research and Development Program of China(No.2023YFC3207901, 2023YFC3207900).

Declarations

Competing interest The authors declare that they have no known competing financial interests or personal relationships that could have appeared to influence the work reported in this paper.

References

1. Xiang, Y., X. Yang, Z. Xu, et al (2020) Fabrication of sustainable manganese ferrite modified biochar from vinasse for enhanced adsorption of fluoroquinolone antibiotics: Effects and mechanisms. Science of the Total Environment 709:136079 http://dx.doi.org/10.1016/j.scitotenv.2019.136079
2. Liao, X., P. Zhao, L. Hou, et al (2023) Network analysis reveals significant joint effects of microplastics and tetracycline on the gut than the gill microbiome of marine medaka. Journal of Hazardous Materials 442:129996 http://dx.doi.org/10.1016/j.jhazmat.2022.129996
3. Ding, D., J. Zhu, Y. Gao, et al (2022) Effect of cattle farm exposure on oropharyngeal and gut microbial communities and antibiotic resistance genes in workers. Science of the Total Environment 806:150685 http://dx.doi.org/10.1016/j.scitotenv.2021.150685
4. Gao, F., H. Zou, D. Wu, et al (2020) Swine farming elevated the proliferation of *Acinetobacter* with the prevalence of antibiotic resistance genes in the groundwater. Environment International 136:105484 http://dx.doi.org/10.1016/j.envint.2020.105484
5. Wang, J., J. Yao, L. Yin, et al (2024) Facet engineering of metal-organic frameworks for efficient tetracycline degradation by photocatalytic activation of peroxymonosulfate. Chemical Engineering Journal 497:154836 http://dx.doi.org/10.1016/j.cej.2024.154836
6. Xing, W., H. Lin, J. Yang, et al (2025) Construction of mixed-dimensional metal-organic frameworks-based heterojunction with enhanced carrier separation for tetracycline degradation by photocatalytic activation of PMS. Journal of Molecular Structure 1336:142085 http://dx.doi.org/10.1016/j.molstruc.2025.142085
7. Miklos, D., C. Remy, M. Jekel, et al (2018) Evaluation of advanced oxidation processes for water and wastewater treatment - A critical review. Water Research 139:118–131 http://dx.doi.org/10.1016/j.watres.2018.03.042
8. Chen, G., Y. Yu, L. Liang, et al (2021) Remediation of antibiotic wastewater by coupled photocatalytic and persulfate oxidation system: A critical review. Journal of Hazardous Materials 408:124461 http://dx.doi.org/10.1016/j.jhazmat.2020.124461
9. Han, D., Z. Song, B. Liu, et al (2026) Mn doping induces oxygen-rich vacancies to regulate Co^{2+} cyclic regeneration and synergistically promote PMS activation and pollutant degradation. Journal of Molecular Structure 1349:143895 http://dx.doi.org/10.1016/j.molstruc.2025.143895
10. Giannakis, S., S. Samoili and J. Rodríguez-Chueca (2021) A meta-analysis of the scientific literature on (photo) Fenton and persulfate advanced oxidation processes: Where do we stand and where are we heading to? Current Opinion in Green and Sustainable Chemistry 29:100456 http://dx.doi.org/10.1016/j.cogsc.2021.100456
11. Adil, S., B. Maryam, E. Kim, et al (2020) Individual and simultaneous degradation of sulfamethoxazole and trimethoprim by ozone, ozone/hydrogen peroxide and ozone/persulfate processes: A comparative study. Environmental Research 189:109889 http://dx.doi.org/10.1016/j.envres.2020.109889
12. Fard, M. and B. Barkdoll (2018) Effects of oxalate and persulfate addition to Electrofenton and Electrofenton-Fenton processes for oxidation of Ketoprofen: Determination of reactive species and mass balance analysis. Electrochimica Acta 265:

209–220 http://dx.doi.org/10.1016/j.electacta.2018.01.153
13. Gao, Y., Q. Wang, G. Ji, et al (2022) Degradation of antibiotic pollutants by persulfate activated with various carbon materials. Chemical Engineering Journal 429:132387 http://dx.doi.org/10.1016/j.cej.2021.132387
14. Zhang, J., S. Yang, K. Zhou, et al (2024) Preparation of co-doped biochar to improve electron transfer and modulate $^1O_2$ generation: Unraveling the radical-unradical mechanism. Chemical Engineering Journal 491:151985 http://dx.doi.org/10.1016/j.cej.2024.151985
15. Song, G., F. Qin, J. Yu, et al (2022) Tailoring biochar for persulfate-based environmental catalysis: Impact of biomass feedstocks. Journal of Hazardous Materials 424:127663 http://dx.doi.org/10.1016/j.jhazmat.2021.127663
16. Wang, J. and S. Wang (2019) Preparation, modification and environmental application of biochar: A review. Journal of Cleaner Production 227:1002–1022 http://dx.doi.org/10.1016/j.jclepro.2019.04.282
17. Wang, S. and J. Wang, 2021. Nitrogen doping sludge-derived biochar to activate peroxymonosulfate for degradation of sulfamethoxazole: Modulation of degradation mechanism by calcination temperature. Journal of Hazardous Materials. 418, http://dx.doi.org/10.1016/j.jhazmat.2021.126309.
18. Huo, Y., H. Zheng, Y. Jiang, et al (2023) Comparison and Characterization of Nitrogen/Sulfur-Doped Activated Carbon for Activating Peroxydisulfate to Degrade Acid Orange 7: An Experimental and Theoretical Study. Industrial & Engineering Chemistry Research 62:11894–11904 http://dx.doi.org/10.1021/acs.iecr.3c01467
19. Xu, C., G. Yang, J. Li, et al (2022) Efficient purification of tetracycline wastewater by activated persulfate with heterogeneous Co-V bimetallic oxides. Journal of Colloid and Interface Science 619:188–197 http://dx.doi.org/10.1016/j.jcis.2022.03.126
20. Qu, J., J. Xue, M. Sun, et al (2024) Superefficient non-radical degradation of benzo a pyrene in soil by Fe-biochar composites activating persulfate. Chemical Engineering Journal 481:148585 http://dx.doi.org/10.1016/j.cej.2024.148585
21. Hou, S., H. Hu, Q. Fu, et al (2024) Undaria pinnatifida (wakame)-derived Fe, N co-doped graphene-like hierarchical porous carbon as highly efficient catalyst for activation of peroxymonosulfate (PMS) toward degradation of tetracycline (TC). Separation and Purification Technology 333:125980 http://dx.doi.org/10.1016/j.seppur.2023.125980
22. Xu, Y., S. Liu, M. Wang, et al (2021) Thiourea-assisted one-step fabrication of a novel nitrogen and sulfur co-doped biochar from nanocellulose as metal-free catalyst for efficient activation of peroxymonosulfate. Journal of Hazardous Materials 416:125796 http://dx.doi.org/10.1016/j.jhazmat.2021.125796
23. Zhang, K., P. Sun, M. Faye, et al (2018) Characterization of biochar derived from rice husks and its potential in chlorobenzene degradation. Carbon 130:730–740 http://dx.doi.org/10.1016/j.carbon.2018.01.036
24. Dai, Z., L. Zhao, S. Peng, et al (2022) Removal of oxytetracycline promoted by manganese-doped biochar based on density functional theory calculations: Comprehensive evaluation of the effect of transition metal doping. Science of the Total Environment 806:150268 http://dx.doi.org/10.1016/j.scitotenv.2021.150268
25. Meng, H., C. Nie, W. Li, et al (2020) Insight into the effect of lignocellulosic biomass

source on the performance of biochar as persulfate activator for aqueous organic pollutants remediation: Epicarp and mesocarp of citrus peels as examples. Journal of Hazardous Materials 399:123043 http://dx.doi.org/10.1016/j.jhazmat.2020.123043.
26. Yin, Q., H. Yan, Y. Liang, et al (2023) Nitrogen doped biochar derived from algae as persulfate activator for the degradation of tetracycline: Role of exogenous N doping and electron transfer pathway. Separation and Purification Technology 318:123970 http://dx.doi.org/10.1016/j.seppur.2023.123970
27. Chen, L., X. Jiang, R. Xie, et al (2020) A novel porous biochar-supported Fe-Mn composite as a persulfate activator for the removal of acid red 88. Separation and Purification Technology 250:117232 http://dx.doi.org/10.1016/j.seppur.2020.117232
28. Huang, D., Q. Zhang, C. Zhang, et al (2020) Mn doped magnetic biochar as persulfate activator for the degradation of tetracycline. Chemical Engineering Journal 391:123532 http://dx.doi.org/10.1016/j.cej.2019.123532
29. Tan, J., X. Chen, M. Shang, et al (2023) N-doped biochar mediated peroxydisulfate activation for selective degradation of bisphenol A: The key role of potential difference-driven electron transfer mechanism. Chemical Engineering Journal 468:143476 http://dx.doi.org/10.1016/j.cej.2023.143476
30. Gong, J., H. Jiang, X. Li, et al (2024) Highly efficient activation of periodate by a manganese-modified biochar to rapidly degrade methylene blue. Environmental Research 241:117657 http://dx.doi.org/10.1016/j.envres.2023.117657
31. Liu, Z., Z. Zhou, G. Qi, et al (2019) Selective catalytic reduction of NO_x with NH_3 over MoO_3/Mn-Zr composite oxide catalyst. Applied Surface Science 466:459–465 http://dx.doi.org/10.1016/j.apsusc.2018.10.081
32. Dong, J., P. Li, X. Ji, et al (2023) Electrons of d-orbital (Mn) and p-orbital (N) enhance the photocatalytic degradation of antibiotics by biochar while maintaining biocompatibility: A combined chemical and biological analysis. Journal of Hazardous Materials 451:131083 http://dx.doi.org/10.1016/j.jhazmat.2023.131083
33. Liu, Z., R. Chen, M. Li, et al (2023) Manganese-nitrogen co-doped biochar (MnN@BC) as particle electrode for three-dimensional (3D) electro-activation of peroxydisulfate: Active sites enhanced radical/non-radical oxidation. Journal of Hazardous Materials 459:132089 http://dx.doi.org/10.1016/j.jhazmat.2023.132089
34. Zhang, R., Z. Lin, J. Chen, et al (2024) Mechanistic insights into delta-MnO_2/biochar-activated persulfate-treated wastewater containing antibiotics and heavy metals: Nonradical pathway and pivotal role of Cu(II) at low temperature. Chemosphere 362:142715 http://dx.doi.org/10.1016/j.chemosphere.2024.142715
35. Zhu, S., X. Huang, F. Ma, et al (2018) Catalytic Removal of Aqueous Contaminants on N-Doped Graphitic Biochars: Inherent Roles of Adsorption and Nonradical Mechanisms. Environmental Science & Technology 52:8649–8658 http://dx.doi.org/10.1021/acs.est.8b01817
36. Yan, D. and I. Lo (2013) Removal effectiveness and mechanisms of naphthalene and heavy metals from artificially contaminated soil by iron chelate-activated persulfate. Environmental Pollution 178:15–22 http://dx.doi.org/10.1016/j.envpol.2013.02.030
37. Liu, G., S. You, Y. Tan, et al (2017) In Situ Photochemical Activation of Sulfate for Enhanced Degradation of Organic Pollutants in Water. Environmental Science &

Technology 51:2339–2346 http://dx.doi.org/10.1021/acs.est.6b05090
38. Duan, X., Z. Ao, L. Zhou, et al (2016) Occurrence of radical and nonradical pathways from carbocatalysts for aqueous and nonaqueous catalytic oxidation. Applied Catalysis B-Environmental 188:98–105 http://dx.doi.org/10.1016/j.apcatb.2016.01.059
39. Chung, C., T. Tobino, K. Cho, et al (2016) Alleviation of membrane fouling in a submerged membrane bioreactor with electrochemical oxidation mediated by *in-situ* free chlorine generation. Water Research 96:52–61 http://dx.doi.org/10.1016/j.watres.2016.03.041
40. Ouyang, D., J. Yan, L. Qian, et al (2017) Degradation of 1,4-dioxane by biochar supported nano magnetite particles activating persulfate. Chemosphere 184:609–617 http://dx.doi.org/10.1016/j.chemosphere.2017.05.156
41. Qi, C., X. Liu, J. Ma, et al (2016) Activation of peroxymonosulfate by base: Implications for the degradation of organic pollutants. Chemosphere 151:280–288 http://dx.doi.org/10.1016/j.chemosphere.2016.02.089
42. Chen, J., W. Hong, T. Huang, et al (2016) Activated carbon fiber for heterogeneous activation of persulfate: implication for the decolorization of azo dye. Environmental Science and Pollution Research 23:18564–18574 http://dx.doi.org/10.1007/s11356-016-7015-4
43. Zhao, Z., J. Wang, J. Pan, et al (2020) Fabrication of Ag_3PO_4/Ag/MoO_{3-x} Z-scheme system with excellent photocatalytic degradation performance under visible light irradiation. Materials Chemistry and Physics 253:123325 http://dx.doi.org/10.1016/j.matchemphys.2020.123325
44. Zheng, D., J. Zou, H. Xu, et al (2023) Efficiency and mechanism of the degradation of ciprofloxacin by the oxidation of peroxymonosulfate under the catalysis of a Fe_3O_4/N co-doped sludge biochar. Chemosphere 325:138387 http://dx.doi.org/10.1016/j.chemosphere.2023.138387
45. Ahmad, S., L. Liu, S. Zhang, et al (2023) Nitrogen-doped biochar (N-doped BC) and iron/nitrogen co-doped biochar (Fe/N co-doped BC) for removal of refractory organic pollutants. Journal of Hazardous Materials 446:130727 http://dx.doi.org/10.1016/j.jhazmat.2023.130727
46. Wang, X., Z. Yang, Y. Jiang, et al (2024) Adsorption and catalytic degradation of phenol in water by a Mn, N co-doped biochar via a non-radical oxidation process. Separation and Purification Technology 330:125267 http://dx.doi.org/10.1016/j.seppur.2023.125267
47. Meng, X., Q. He, T. Song, et al (2022) Activation of peroxydisulfate by magnetically separable rGO/$MnFe_2O_4$ toward oxidation of tetracycline: Efficiency, mechanism and degradation pathways. Separation and Purification Technology 282:120137 http://dx.doi.org/10.1016/j.seppur.2021.120137
48. Wang, Q., S. Zheng, W. Ma, et al (2024) Facile synthesis of direct Z-scheme PPy/NH_2-UiO-66 heterojunction for enhanced photocatalytic Cr(VI) reduction, industrial electroplating wastewater treatment, and tetracycline degradation. Applied Catalysis B-Environment and Energy 344:123669 http://dx.doi.org/10.1016/j.apcatb.2023.123669
49. Song, T., Y. Gao, J. Ye, et al (2023) Insight into enhanced degradation of tetracycline over peroxymonosulfate activated via biochar-based nanocomposite: performance and mechanism. Environmental Science and Pollution Research 30:27394–27408

http://dx.doi.org/10.1007/s11356-022-24102-5
50. Liu, C., S. Mao, H. Wang, et al (2022) Peroxymonosulfate-assisted for facilitating photocatalytic degradation performance of 2D/2D WO_3/BiOBr S-scheme heterojunction. Chemical Engineering Journal 430:132806 http://dx.doi.org/10.1016/j.cej.2021.132806
51. Zhang, S., C. Lu, Y. Wang, et al (2024) LED-driven photocatalytic degradation of tetracycline by chromite ore processing residue (COPR): Mechanism, pathway, toxicity assessment. Journal of Cleaner Production 434:140384 http://dx.doi.org/10.1016/j.jclepro.2023.140384